D3.3. Thermal shock interface "Thermo-mechanical Behaviour of the Sealant-steel Interface under Thermal Cycling for CCS"

CEMENTEGRITY Deliverable 3.3, v. 1
Published 2025-02-1

Authors: Li, K., Friebel, M., Pluymakers, A.
Rock Mechanics Lab, Delft University of Technology, the Netherlands

Reviewed by: Reinier van Noort (IFE Technology, Norway)

Keywords: *CCS; Sealants; Thermal cycling; Sealant-steel bonding; Thermo-mechanical behaviour*

Summary:

In CCS wells, cyclic injection of cold CO2 into the hot subsurface may lead to debonding between sealant and steel casing. We test how thermal cycling affects the sealing ability of five different types of sealant (S1 to S5) surrounding a simulated steel wellbore. We use cylindrical sealant samples with a stainless steel (AISI 316L) pipe in the centre, cured at 150°C and 30 MPa for 28 days. Using 3 bar N2 leak tests at room temperature, we test how much the sealant-steel interface leaks before and after thermal cycling under unconfined and confined (1.5 MPa) conditions. We also conduct push-off experiments using a 500 kN loading frame before and after. For the unconfined test, we place the sample on a custom-built jig, whereas for confined tests we have a similar assembly inside a conventional triaxial vessel. The samples are brought to 60˚C. Subsequently, we inject 5°C water through the central pipe at 80 mL/min for 2 mins, and let the sample reheat for 12 mins. We repeat this 16 times. Afterwards, we allow the sample to cool to room temperature, and repeat the N2 leak test in-situ. The results show that under unconfined conditions, the interface leaks more for all sealant types except S3. The key parameter controlling performance is the linear thermal expansion coefficient, where an expansion coefficient closer to that of steel indicates better performance. Under confinement, all sealant types perform better post-thermal cycling, due to the prolonged exposure to confining pressure.

Publication status:
This manuscript is under review at Geomechanics for Energy and the Environment

1 Introduction

In carbon capture and storage (CCS), the in-situ temperatures at storage depths between 2 and 4 kilometers typically range from 60°C to 120°C (Eiken et al., 2011; Lescanne et al., 2011; Yoo et al., 2013). However, the temperature of injected CO_2 can be as low as 5°C, particularly in offshore projects (such as the Dutch Portos project or the Norwegian Northern Lights project), where CO_2 is transported to the injection point on the sea-floor using pipelines. This suggests that the periodic injection of cold CO_2 into the warmer subsurface could induce temperature fluctuations of up to 115°C. Under such temperature fluctuations, the wellbore and subsurface formations may experience repeated shrinkage during cold CO_2 injection and subsequent expansion after injection when the system equilibrates back to reservoir temperature. As a result, formation of leakage pathways may occur, which potentially includes fractures within the sealant itself (Carey et al., 2007; Roy et al., 2016; Vilarrasa and Rutqvist, 2017; Li and Pluymakers, 2014a), and/or debonding between sealant sheath and casing due to the mismatch in their thermo-mechanical properties (Albawi et al., 2014; De Andrade et al., 2015; Lund et al., 2015). Given that the wellbore provides the shortest path from the storage reservoir to the surface, the formation of such wellbore-related leakage pathways would pose significant risks to the long-term viability of CO_2 storage underground (Celia et al., 2005). Therefore, understanding the effects of thermal cycling on the integrity of the sealant sheath and on the annulus between sealant and wellbore steel is crucial to ensuring the security and thus long-term sustainability of CO_2 storage systems. Understanding the key properties determining performance will also be fundamental to the design of more resilient sealant compositions that can withstand the dynamic temperature conditions in future CCS.

In most depleted oil and gas wells considered for CCS ("legacy wells"), ordinary Portland cement (OPC) is the most common sealant, due to its effective performance as a zonal isolation material and low cost (Parker et al., 2009; Lesti et al., 2013). However, the sealing integrity of OPC-based sealants can be compromised under thermal fluctuations induced by cyclic CO_2 injection and subsequent storage. Albawi et al. (2014) investigated the impact of thermal cycling on wellbore integrity using micro-computed tomography (micro-CT). Their scaled-down model, consisting of casing pipe, OPC-based sealant, and rock, revealed that slow temperature variations of 75°C caused debonding at the sealant-steel and sealant-rock interfaces, creating leakage pathways up to several millimeters wide in a cm-scale system. Lund et al. (2015) simulated the study by Albawi et al. (2014) and found that the thermal properties of the casing, sealant, and rock significantly influenced the wellbore integrity during thermal cycling. They concluded that large temperature fluctuations could induce sufficient thermal stresses to damage the sealant. Similarly, De Andrade et al. (2015) replicated Albawi et al. (2014)'s experiments and identified shear failure as the primary mechanism for debonding at interfaces. They also noted that shale exhibited better resistance to thermal cycling than sandstone due to its higher stiffness, making it less prone to shear failure.

Besides OPC-based sealants, novel compositions with modified thermo-mechanical properties are gaining more attention for CCS purposes in recent years, such as calcium aluminate cement (CAC)-based and geopolymer-based sealants. CAC possesses higher early strength and greater heat of hydration compared to OPC (Barborak, 2010), making it a promising candidate for CCS applications. In addition, Dugonjic-Bilic et al. (2011) evaluated a CAC-based sealant composition with a retarder in a CO_2 environment and found it effective in controlling water loss, which is beneficial for CCS. Geopolymer-based sealants are becoming increasingly recognized in the wellbore community, because they can be synthesized from waste materials such as fly ash and biomass ash (Nasvi et al., 2014; Freire et al., 2022), making their obtainment eco-friendly. They exhibit favorable properties such as high ductility, low shrinkage, and strong resistance to carbonation (Hajiabadi et al., 2023), hence show great potential for future CCS applications. However, the performance of these two types of sealants under thermal cycling relevant for CCS is currently unexplored. In this paper, we investigate five sealant compositions, labeled S1 through S5 using novel methodologies. For reference purposes, these include two conventional OPC-based sealants, commonly used in aged oil

and gas reservoirs targeted for CCS (S1 and S2), as well as more novel sealants designed for future CCS (S3 to S5). S1 and S2 are standard OPC-based blends, where S2 contains an expansion agent and demonstrates ultra-low permeability for field applications. S3 is also OPC-based but incorporates CO_2-sequestering additives and hence possesses modified mechanical properties. S4 is a CAC-based blend specifically formulated for high acid resistance in a CO_2 storage environment. S5 is a granite-based geopolymer blend with enhanced carbonation resistance for CCS. These are the same sealants previously tested by Li and Pluymakers (2024a and b) and van Noort et al. (2024a and b). S1 through S5 possess a significantly different thermo-mechanical properties, spanning a wide range in tensile and compressive strengths, thermal expansion coefficient, and thermal diffusivity, etc.

To examine the thermo-mechanical behaviour of the sealant-steel interface specifically, we conduct thermal-cycling experiments on cylindrical sealant samples with a steel pipe in the middle. These composite samples are custom-designed to mimic the sealant sheath surrounding the steel casing in a wellbore, whilst still having dimensions that fit a conventional triaxial apparatus. Our experiments are performed either without confinement (worst case scenario) or at a relatively low confinement of 1.5 MPa. Under in-situ conditions, confining pressure can reach tens of MPa, depending on the CO_2 storage depth (Kirby et al., 2001; Alnes et al., 2011). We also performed tests under unconfined conditions to represent the worst-case scenario and evaluate whether the added experimental complexity of confinement is worth the additional time required for testing. Note that the thermal cycling used in this study is on the extreme side: we apply an instantaneous temperature drop of 55˚C with 12 min intervals between cycles. Whilst the absolute temperature difference is plausible for a scenario where cold CO_2, transported over the seafloor is injected into a hot reservoir, the rapid temperature change and short cycle intervals are atypical in an engineering scenario. Moreover, the number of cycles in our experiments is limited to a maximum of 16. Mechanics dictates that more loading cycles lead to greater damage accumulation (Miner, 1945; Fatemi and Yang, 1998; Suresh, 1998). Regardless, we use our bespoke sample type, assembly and experimental protocol to investigate which thermo-mechanical properties control the performance of the sealant-steel interface in a thermomechanical regime resembling CO_2 storage conditions.

2 Experimental Materials, Apparatus, and Methodologies

2.1 Sample description

In our study, we employ composite samples with cylindrical sealant sheath (diameter 3 cm, length 7 cm) bonded to a steel pipe (ID 4 mm, wall thickness 1 mm, AISI 316L stainless steel, Swagelok Nederland) in the centre to mimic the wellbore section. As shown in Fig. 1, the steel pipe sticks 1.5 cm out of both ends of the sealant sheath.

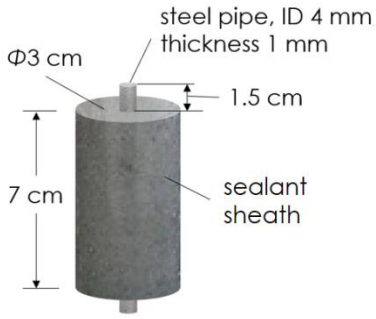

Fig. 1. Schematic of the composite sample.

We test five sealants of different compositions as shown in Table 1, which includes their Technology Readiness Levels (TRLs) defined by API (2009). These compositions include conventional sealants representative in aged oil and gas reservoirs targeted for CCS (S1 and S2), and more novel sealants newly designed for future CCS (S3 to S5). S1 and S2 are standard OPC-based blends, where S2 exhibits an ultra-reduced permeability for field design. S3, designed by Restone (Kvassnes and Clausen, 2020; 2021) is also OPC-based but with CO_2-sequestering additives and modified mechanical properties. S4 is a CAC-based blend specifically designed to be highly acid resistant for CO_2 storage environment. S5, designed University of Stavanger (Hajiabadi et al., 2024), is a geopolymer-based blend with high resistance against carbonation for CCS.

Sealant	Composition	TRL
S1	1.90 SG class G cement with 35% BWOC silica flour	7: Proven technology
S2	1.90 SG ultra-reduced permeability class G cement with 35% BWOC silica flour, with high silica fume concentration and expansion agent in form of dead-burnt MgO	7: Proven technology
S3	1.90 SG class G cement with 35% BWOC silica flour, with silica fume, expansion agent in form of dead-burnt MgO, and CO_2-sequestering additives based on olivine minerals	3: Prototype tested
S4	1.80 SG highly acid-resistant calcium aluminate-based blend	7: Proven technology
S5	1.90 SG granite-based (feldspar rich type of rock as a precursor) geopolymer for CCS	3: Prototype tested

Table 1: an overview of four sealant compositions and their TRLs. Thermomechanical properties are in Table 2.

S1 to S4 are also used by Li and Pluymakers (2024), who worked on the same sealant batch, but with sample configurations and a protocol targeting the thermomechanical performance of the sealant material alone. All samples are cast and cured by Halliburton AS Norway, following API Recommended Practice 10B-2 (API RP 10B-2 (2013)). Sealant slurry is mixed with a water/cement ratio of 0.4, and cast into a Teflon mould with a steel pipe (AISI 316L) pre-mounted as the central axis of the sample cylinder. Then the whole sample is cured at 150°C and 30 MPa for 28 days. Under such elevated temperature and pressure during curing, the chemical reactions of the sealant and the bonding process between the sealant sheath and the steel pipe will be near completion during the curing itself. This minimizes variation in the mechanical and thermal properties of our samples in the time between curing and usage. They are stored in fresh water at room temperature and pressures throughout the study period. Unconfined Compressive Strength tests performed at 1 month intervals confirm that mechanical properties do not evolve during storage (see also Li and Pluymakers, 2024). Before use, the samples are dried in an air-circulated oven (model UF75, Memmert) at 60°C (ramping rate of 0.5°C/min from room temperature to 60°C). Afterwards, the samples are completely dry, which is confirmed by no weight reduction after two days. Note that the slow ramping rates minimizes the damage induced by the drying process, since thermal stresses that built up during heating and cooling have time to slowly dissipate instead of leading to mechanical damage. This is confirmed by microtomography measurements of the samples before thermal cycling.

2.2 Pre- and post-thermal cycling thermomechanical analysis

The thermomechanical properties of S1 to S4 are reported by Li and Pluymakers (2024). In this study, we also report the mechanical and thermal properties of post-curing and post-drying sealant S5 before any thermal-cycling experiments, performed in the exact same manner as the previously reported

measurements on S1 to S4. To summarize, we used a 500 kN loading frame to conduct uniaxial compressive tests on 3 solid cylindrical S5 samples (diameter 3 cm, length 7 cm) to measure the unconfined compression strength (UCS), Young's modulus, and Poisson's ratio. We used a 50 kN loading frame to conduct Brazilian disc tests on S5 disc samples (diameter 3 cm, thickness 1.5 cm) to measure the indirect tensile strength. Bulk density of S5 is calculated by the weight of the sample (weighed using a laboratory balance, Model VIC-303, Acculab Sartorius Group) divided by its volume. A thermal constants analyzer (Hot Disk® TPS 2200) is used to measure the thermal conductivity and specific heat capacity. Then thermal diffusivity of sealant S5 is calculated by thermal conductivity divided by density and specific heat capacity. In addition, we used a thermomechanical analyzer (PerkinElmer, TMA 4000) to measure the linear thermal expansion coefficient and a helium gas pycnometer (Anton Paar, Ultrapyc 5000) to measure the effective porosity. All thermomechanical properties are provided in Table 2.

Sealant	Unconfined compressive strength [MPa]	Young's modulus [GPa]	Poisson's ratio [-]	Tensile Strength [MPa]	Bulk density [kg/m^3]	Thermal conductivity [W/(m·K)]	Specific heat capacity [J/(kg·K)]	Thermal diffusivity [mm^2/s]	Linear thermal expansion coefficient [10^{-6} K^{-1}]	Effective porosity by helium pycnometer [%]
S1	99.8 ±1.1	13.4 ±0.2	0.143 ±0.005	3.63 ±0.35	1455	0.82 ±0.04	878 ±18	0.64	6.89 ±0.20	35.6 ±1.9
S2	81.1 ±1.3	12.0 ±0.2	0.162 ±0.010	5.51 ±0.32	1507	0.93 ±0.03	936 ±11	0.66	10.93 ±0.62	26.8 ±2.1
S3	33.4 ±0.7	6.1 ±0.1	0.139 ±0.009	6.79 ±0.15	1374	1.04 ±0.02	684 ±13	1.11	9.40 ±0.12	42.2 ±0.9
S4	34.3 ±1.3	6.6 ±0.1	0.172 ±0.014	3.92 ±0.10	1497	0.89 ±0.02	970 ±21	0.61	12.32 ±0.53	37.5 ±1.6
S5	61.4 ±2.07	9.5 ±0.39	0.163 ±0.001	8.11 ±0.24	1417	0.79 ±0.02	527 ±23	1.06	8.15 ±0.14	35.5 ±0.9

Table 2: mechanical and thermal properties of the five sealants, as measured before thermal treatment. Note that properties of sealants S5 are measured in this study. Those of S1 to S4 were measured by by Li and Pluymakers (2024a and b).

In our study, we also designed bespoke push-off experiments on intact composite samples of sealants S1 to S5 to quantify the strength of the bonding between the sealant sheath and the steel pipe. This has some similarity to conventional bond strength measurements on steel-sealant interfaces (Suryanto et al, 2024), but the geometry of our composite samples differs. As shown in Fig. 2, we mount reference composite samples (i.e. that have not undergone any thermal cycling) on our 500 kN loading frame, which is fit with a customized steel top cap with similar bottom base. The outer surface of the sealant sheath is not in contact with the inner surface of either cap. We apply loading in displacement control mode (rate of 0.0005 mm/s) to push the pipe from the top off the sealant sheath while the sheath is supported by the bottom base, i.e. similar to a standard UCS test. We record the force profile against the displacement of the pipe to obtain the push-off force F_{po} beyond which the force gets stable or slowly decreases in spite of further displacement. We then calculate the push-off shear stress σ_{po} through division of the push-off force by the bonding area A_b between sealant sheath and the steel pipe. The equation is given below,

$$\sigma_{po}\ \frac{F_{po}}{A_b} = \frac{F_{po}}{\pi\, d\, H} \tag{1}$$

where d is outer diameter of the steel pipe (6 mm), and H is the length of the sealant sheath (7 cm).

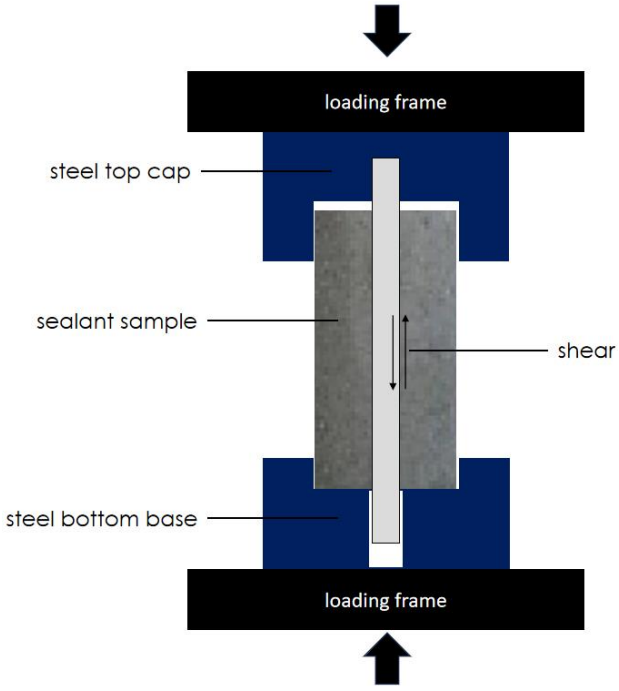

Fig. 2. Schematic of experimental setup for push-off experiments on composite samples. The drawing does not adhere to the actual scale.

To ensure our procedures are reliable and we obtain repeatable measurements, we conduct push-off experiments on three intact samples (post-curing and post-drying, but without thermal treatment) for each sealant S1 to S5. These three measurements per each sealant are obtained at one month intervals during three months. We also perform similar push-off experiments to all composite samples after thermal treatment to study how thermal cycling affects the mechanical efficacy of the bonding at the sealant-steel interface.

To further determine how thermal cycling affects the integrity of our composite samples including sealant sheath and bonding between sealant sheath and steel pipe, we scan one sample per each sealant S1 to S5 after thermal treatment in unconfined experiments using a micro-CT scanner (CoreTOM, TESCAN UniTom XL, voxel resolution of 32 μm). Images are post-processed with Panthera software (version 1.4, TESCAN) to detect the possibility of crack formation in sealant or de-bonding at sealant-steel interface after the experiments. Due to technical limitations, any cracks smaller than 32 µm cannot be detected (i.e. the voxel size), nor would any aperture be visible close to the steel pipe due to the high density of the steel compared to the sealant.

2.3 Thermal cycling procedure

In our study, we carry on thermal cycling experiments on composite samples of sealants S1 to S5 either without or with 1.5 MPa confinement. All composite samples tested in this study and the experimental scheme are outlined in Table 3.

2.3.1 Unconfined experiments

For the unconfined experiments we designed a jig, shown in Fig. 3. To mount the sample, we first apply a 5 mm-thick layer of hardened glue (cured under ambient conditions for two days, industrial adhesives 3720A, Permacol B.V.) on the outer surface of the sealant sheath of the sample (1.5 cm height from both ends). We then firmly attach the composite sample with customized steel top cap and bottom base with built-in flowlines. The whole sample assembly is then secured by three bolts over the entire assembly length and placed in an laboratory oven (model UF75, Memmert).

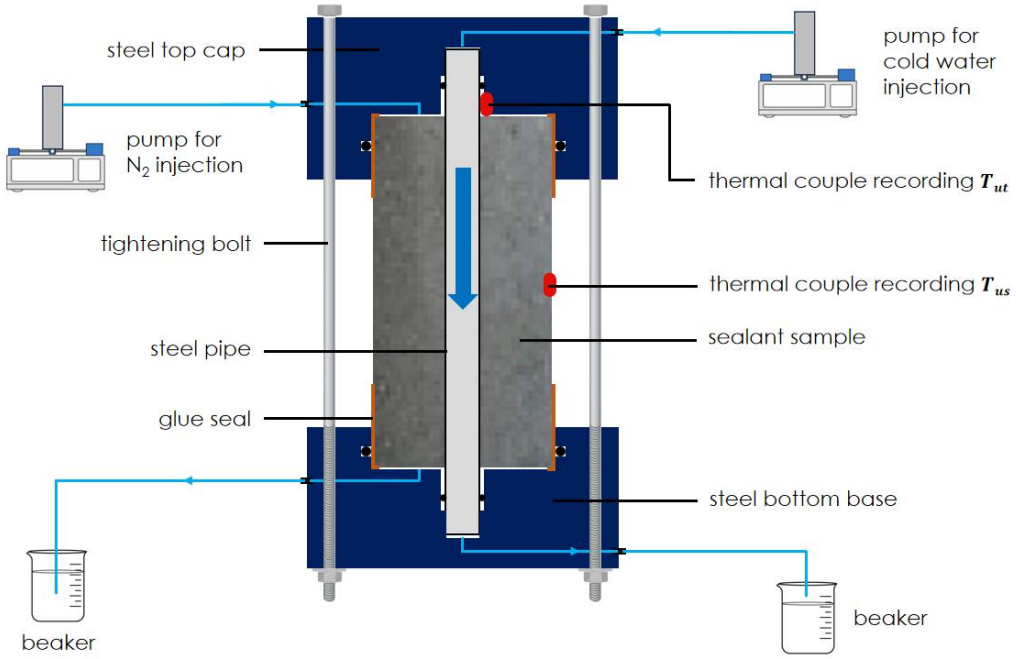

Fig. 3. Schematic of experimental setup for unconfined thermal-cycling experiments. The setup is placed in an laboratory oven. The drawing does not adhere to the actual scale.

During the unconfined experiment, we first use a syringe pump (model 1000D, Teledyne ISCO, range: 0.001 to 408 mL/min, accuracy: 0.5% of setpoint) to apply 3 bar N_2 on the top surface of the sealant sheath for 30 mins without confinement and at room temperature. We monitor the volume decrease of N_2 after 30 mins, based on which we calculate the penetration rate, which will occur through the matrix of sealant sheath as well as the sealant-steel interface. We apply leak detector solution (Swagelok Snoop) on the seams between sealant sheath and the steel caps, as well as on the joints of flowlines to ensure the N_2 doesn't leak. When there is no bubble foam observed, it confirms there is no leakage from the sample assembly and we proceed with the next steps. We then heat the whole sample assembly (unjacketed and unconfined) at a ramping rate of 1.3°C/min to 60°C. Then the sample assembly is maintained at this temperature for 30 mins to be fully heated. We next use another syringe pump (model 1000D, Teledyne ISCO) to inject 5°C water at a rate of 80 mL/min for 2 mins through the steel pipe of the sample from top to bottom to apply a rapid temperature drop. We then halt for 12 mins before the next injection to allow the sample assembly to re-equilibrate back to 60°C. We repeat the injection followed by reheating for 16 cycles. As shown in Fig. 3, two thermocouples (type K, NI-9219, National Instruments rated to 700 °C with an accuracy ±1 °C) are installed to measure the temperature during the experiment on the outer surface in the sample centre (T_{us}), as well as on the top surface of the sealant sheath adjacent to the steel pipe (T_{ut}). After the thermal treatment, we allow the sample assembly to cool down to room temperature naturally. Then we apply 3 bar N_2 on the top surface of the sealant sheath for 30 mins again, to calculate the post-treatment N_2 penetration rate. Combined with the additional post-treatment shear-off experiment, we deem this in-house designed protocol sufficient to study the effects of thermal cycling on the integrity of the sealant sheath and sealant-steel interface. We test two samples for each sealant composition of S1 to S5.

2.3.2. Confined experiments

In confined experiments, we use a standard triaxial deformation apparatus (Figure 4), where a composite sealant sample is placed in a pressure vessel. The confining pressures can be maximum 70 MPa, and axial force can be maximum up to 300 kN (equivalent to 442 MPa axial stress on our composite sample). As

shown in Fig. 4, it is equipped with an internal furnace. During the experiments, the triaxial vessel is filled with heat transfer oil (Shell Thermia oil B) that provides the confining pressure and transmits the heat. During thermal cycling experiments, a water bath is running through the annulus in the vessel shell to cool and protect the electronics of the apparatus from elevated temperature.

The sample, jacketed by a heat-shrinkable FEP (fluorinated ethylene propylene) tube (thickness 0.5 mm), is mounted between the upper and lower axial pistons. In both pistons, flowlines are fitted to allow water injection through the steel pipe of the composite sample. Moreover, there are additional flow lines to provide access to the sealant surface, similar to the unconfined experiments. Two high-precision linear variable differential transformers (LVDTs, 2 mm range) mounted parallel to the sample, and one circumferential strain gauge (10 mm range) mounted around the sample are used to monitor axial and radial deformation, respectively. Two thermocouples (same model as used in unconfined experiments) are installed to measure the temperature on the outer surface in the sample centre (T_{cs}), as well as on the top surface of the sealant sheath adjacent to the steel pipe (T_{ct}).

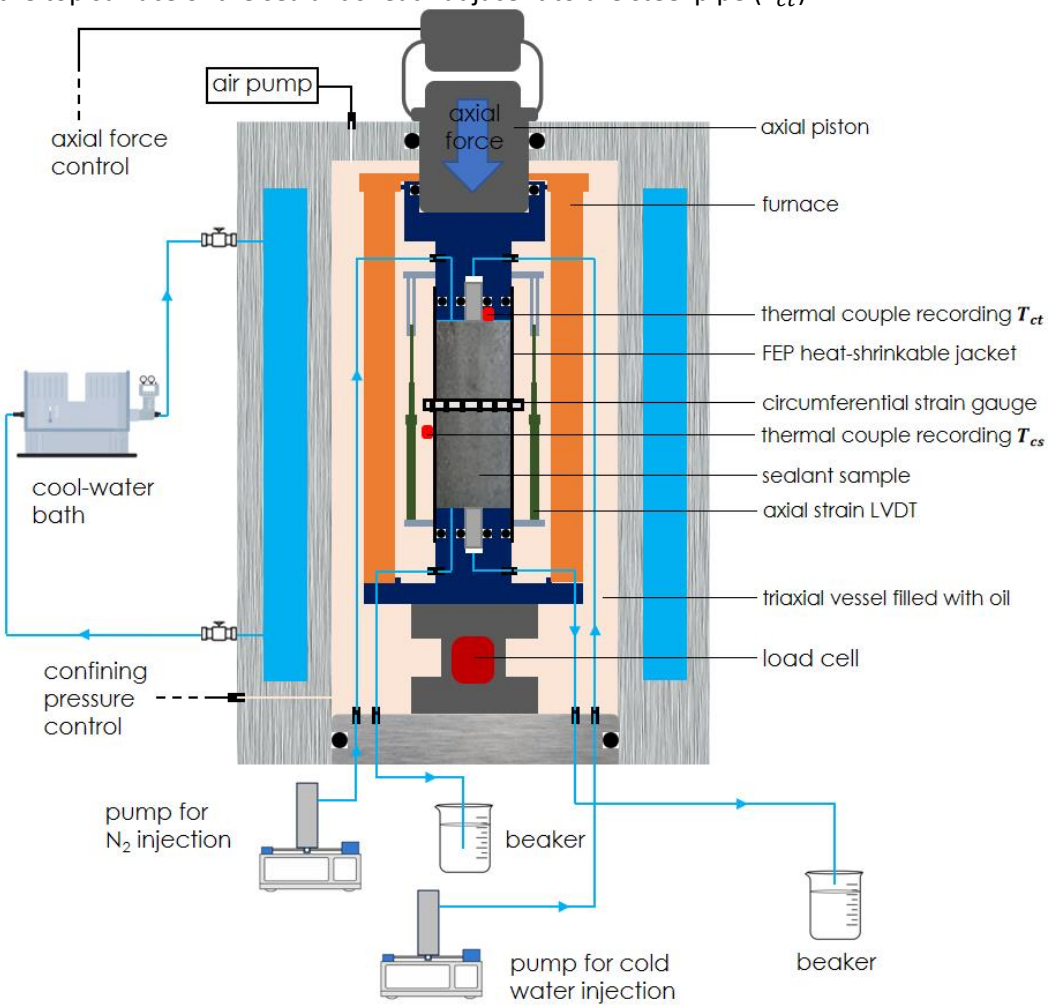

Fig. 4. Schematic of experimental setup for confined thermal-cycling experiments. The setup is a standard triaxial deformation apparatus with the composite sample mounted inside the pressure vessel. The drawing does not adhere to the actual scale.

In confined thermal-cycling experiments, to mimic an in-situ state of stress, we load the sample close to a hydrostatic condition at a confining pressure of 1.5 MPa with an axial stress of 4 MPa. Then similar to unconfined experiments, we use a syringe pump (model 260D, Teledyne ISCO, range: 0.001 to 107

No.	Sample name	Sealant composition	Confinement	Experiment type	Experimental scheme
1	S1C-1	S1, OPC blend	0 MPa	unconfined thermal-cycling experiment	3 bar N_2 penetration test ↓ thermal cycling ↓ 3 bar N_2 penetration test ↓ micro-CT (on one sample per each sealant) ↓ push-off shear experiment
2	S1C-2				
3	S2C-1	S2, OPC blend with ultra-reduced permeability			
4	S2C-2				
5	S3C-1	S3, OPC blend with CO_2-sequestering additives			
6	S3C-2				
7	S4C-1	S4, CAC blend			
8	S4C-2				
9	S5C-1	S5, geopolymer blend			
10	S5C-2				
11	S1C-3	S1, OPC blend	1.5 MPa	confined thermal-cycling experiment	confinement loading ↓ 3 bar N_2 penetration test ↓ thermal cycling ↓ 3 bar N_2 penetration test ↓ confinement unloading ↓ push-off shear experiment
12	S2C-3	S2, OPC blend with ultra-reduced permeability			
13	S3C-3	S3, OPC blend with CO_2-sequestering additives			
14	S4C-3	S4, CAC blend			
15	S5C-3	S5, geopolymer blend			
16	S4C-4	S4, CAC blend		reference loading experiment	same as for confined thermal-cycling experiment, only without thermal-cycling treatment
17	S5C-4	S5, geopolymer blend			

Table 3: an overview of all composite samples to be tested and the experimental scheme.

mL/min, accuracy: 0.5% of setpoint) to apply 3 bar N_2 to the top surface of the sealant sheath for 30 mins while the composite sample is under 1.5 MPa confinement and room temperature. The penetration rate of N_2 through the matrix of sealant sheath and the sealant-steel interface is then calculated. Afterward we heat the pressure vessel to 60ºC at a ramping rate of 1.3°C/min (whilst maintain 1.5 MPa confining pressure), and allow temperature to equilibrate for 30 min, to allow the sample assembly to be heated through and through. We apply the same thermal cycling protocol as in the unconfined experiments. In 16 cycles, we inject 5ºC water from top to bottom through the central steel pipe using a syringe pump (model 1000D, Teledyne ISCO; 80 mL/min for 2 mins). Then we pause 12 min before the next cycle starts.

Afterwards, we shut down the furnace and the temperature of the system gradually decreases to room temperature overnight whilst maintaining 1.5 MPa confining pressure. Subsequently, we perform the 30 min post-treatment penetration test. This is followed by unloading. Afterward the sample is retrieved and the post-treatment push-off experiment is performed. Due to the complexity of the procedure, only one sample can be tested for each sealant composition. However, in addition, we carry out reference experiments to investigate the effects of confinement alone. We use the triaxial deformation apparatus to apply 1.5 MPa confinement and 4 MPa axial stress on the composite sample without thermal treatment. These experiments are conducted at room temperature and the duration of the application of confining pressure is 6 hrs, the same as in confined thermal-cycling experiments (see Fig. 6). We test one sample for sealant S4 and S5. After the reference loading experiments, we perform push-off experiments on these two composite samples.

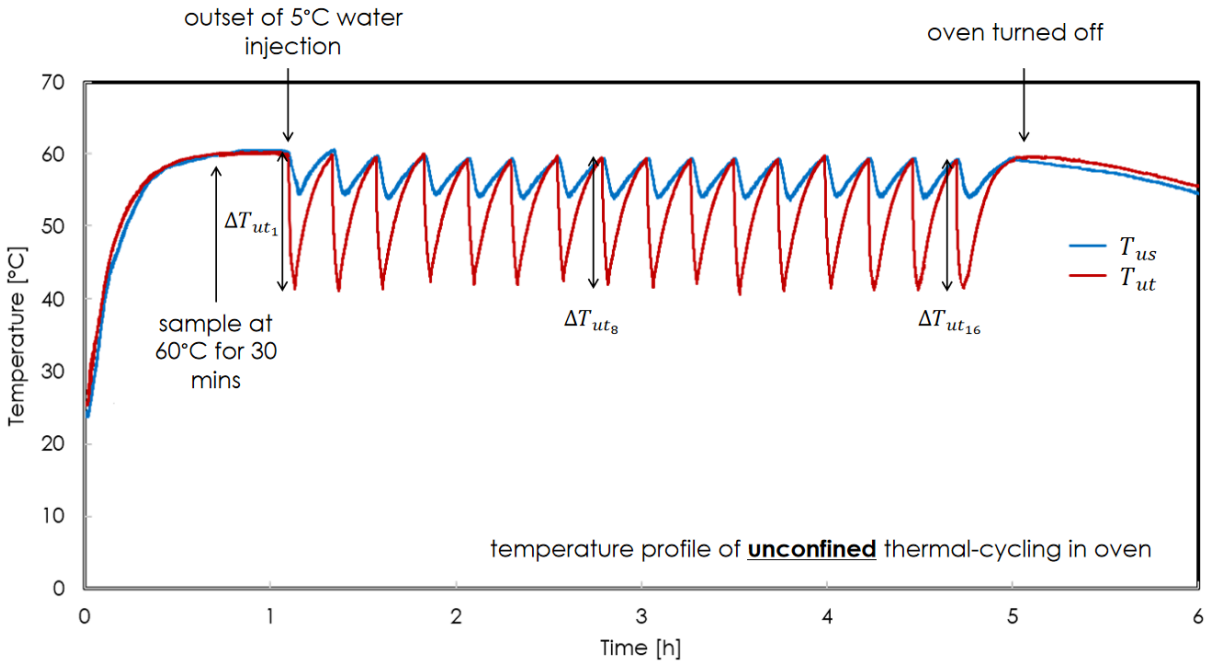

Fig. 5. Temperature variations at the outer surface in the sample centre (T_{us}), as well as on the top surface of the sealant sheath adjacent to the steel pipe (T_{ut}) of composite sample S1C-1 during unconfined thermal-cycling experiment. These variations are representative for all unconfined thermal-cycling experiments conducted on two samples per each sealant S1 to S5 (see Table 3).

3 Results and Discussions

3.1 Temperature profile and thermal stress

Fig. 5 illustrates the temperature variations at the different positions of sample S1C-1 during a representative unconfined thermal-cycling, and Fig. 6 illustrates the temperature variations at the different positions of sample S1C-3 during a representative confined thermal-cycling experiment. In Fig. 6, the circumferential strain, ε_θ, of the composite sample S1C-3 throughout the experiment duration is also plotted. As depicted in both Figs., temperatures on the outer surface, T_{us} or T_{cs}, and on the top surface, T_{ut} or T_{ct}, of the samples reach 60ºC after the initial gradual heating. These temperatures remain constant at 60ºC until thermal cycling commences. Upon initial water injection, T_{ut} and T_{ct} quickly decrease to 41ºC and 45ºC respectively within 2 minutes, while T_{us} and T_{cs} decreases to 55ºC and 57ºC. The discrepancy in temperature drop between unconfined and confined experiments arises primarily from the difference in experimental procedure. There is a diminished temperature drop experienced under confinement during thermal cycling, since in the triaxial deformation setup (Fig. 4), the path that

the injected water must traverse through the apparatus to reach the sample is relatively long, which means that the water that reaches the sample is not 5 ºC anymore. Nonetheless, in both cases, the temperature drops are significant. After cold water injection is halted, all temperatures equilibrate back to the system temperature at 60 ºC within 12 minutes, and the system is ready for the next cycle.

In the confined experiment (Fig. 6), throughout the whole process, sample S1C-3 is exposed to 1.5 MPa confinement, and circumferential strain is tracked. The sample exhibits an overall decrease in circumferential strain, indicating compaction, with superimposed fluctuations that are in tune with the temperature fluctuations at the outer surface T_{cs}.

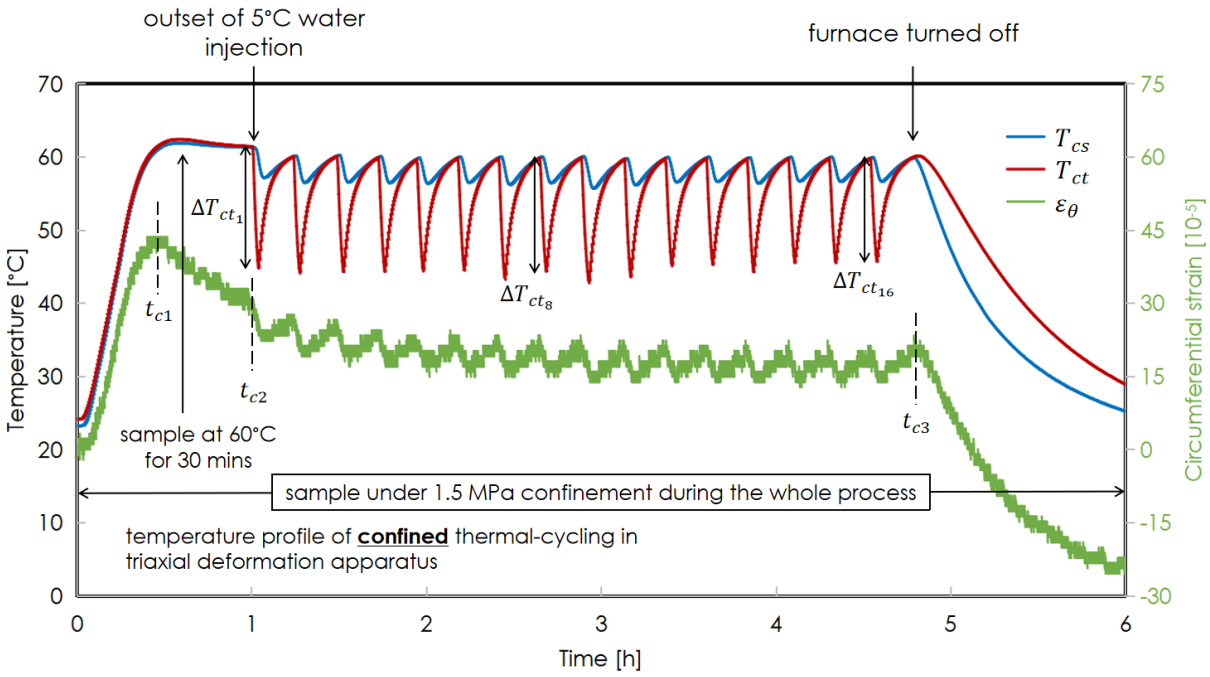

Fig. 6. Temperature variations at the outer surface in the sample centre (T_{cs}), as well as on the top surface of the sealant sheath adjacent to the steel pipe (T_{ct}) of composite sample S1C-3 during confined thermal-cycling experiment. The circumferential strain, ϵ_θ, of the sample throughout the experiment duration is also plotted. These variations serve as a representation for for confined thermal-cycling experiments conducted on one samples per each sealant S1 to S5 (see Table 3).

As shown in Figs. 5 and 6, the most significant temperature fluctuation on the sealant sheath of the composite samples is observed on its top surface adjacent to the steel pipe, which is ΔT_{ut_i} for unconfined experiments, or ΔT_{ct_i} for confined experiments respectively; i is the order of the thermal cycling. At this position of the sealant sheath, the thermal cycling induces the highest thermal stress throughout the sample. We determine this maximum thermal stress either in unconfined or confined experiments, $\sigma_{T_{u,c}}$, using the below equation (Carter and Paul, 1991; Callister et al., 2007):

$$\sigma_{T_{u,c}} = E \cdot \gamma \cdot \Delta T_{ut,ct} \quad (2)$$

where E is Young's modulus, γ the thermal expansion coefficient of the sealant, and $\Delta T_{ut,ct} = \frac{\sum_1^{16} \Delta T_{ut_i,ct_i}}{16}$ is the average temperature drop on the top surface of the sealant sheath adjacent to the steel pipe of the sample within one injection cycle.

3.2 Thermo-mechanical behaviour under unconfined thermal cycling

Figure 7 presents 3 bar N_2 penetration rates of composite samples of sealants S1 to S5 (two samples per each sealant) before and after unconfined thermal-cycling experiments. Penetration rates increase after

thermal treatment for samples of all sealants except S3. For S3, the post-treatment changes of penetration rate are insignificant. These indicate that thermal cycling has induced leaking effects on samples for all sealants except S3 through either the matrix of sealant sheath, or the sealant-steel interface, or both. The consistency in results from the two samples for each sealant S1 to S5 ensures that our experimental design (Fig. 3) and protocols are reliable and reproducible. Compared to S2 and S4, samples of sealants S1 and S5 experience a more significant increase in penetration rate, meaning that the thermal-induced leaking effect is more severe for samples of these two sealants. Note that, even though the qualitative trends are similar, the absolute penetration rates pre- and post-thermal treatment are different, indicating that overall there is also significant initial variation in the bond quality.

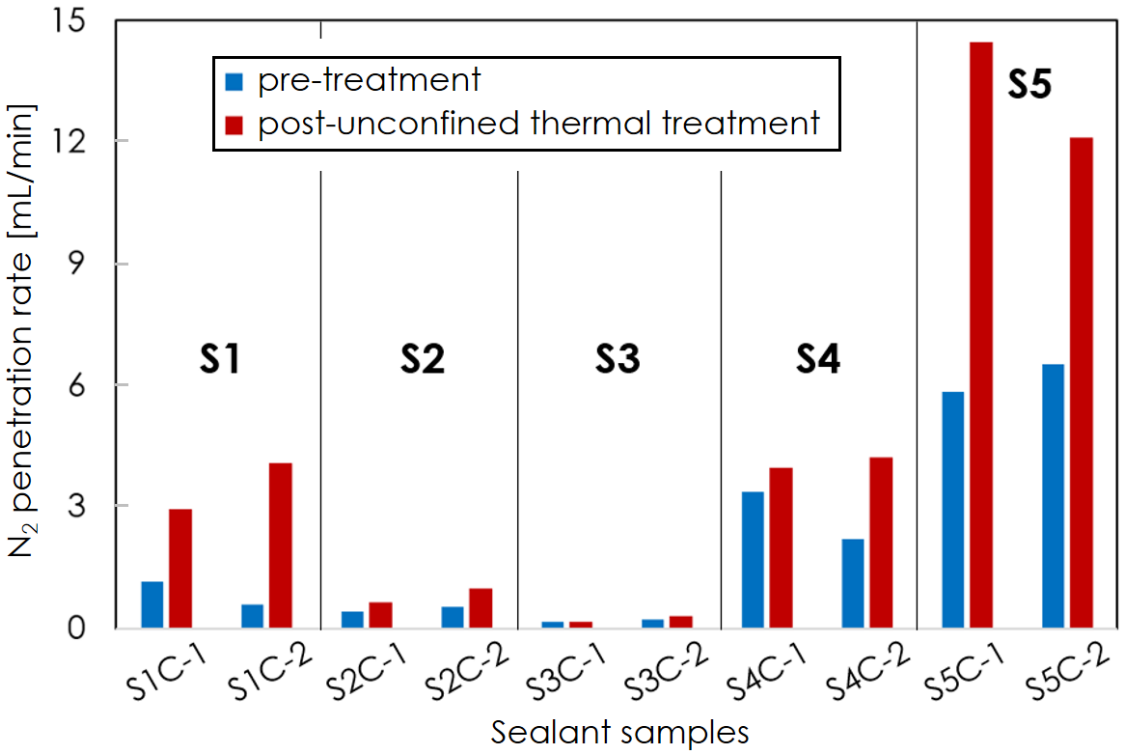

Fig. 7. N_2 penetration rates of composite samples of sealants S1 to S5 (two samples per each sealant) before and after unconfined thermal-cycling experiments.

Figure 8 displays micro-CT images of S1 to S5 samples after unconfined thermal-cycling experiments. This shows there are no cracks in the sealant sheath for any of the samples following the thermal treatment, in line with the expectations based on Li and Pluymakers, submitted. However, it is challenging to evaluate the bonding integrity of sealant-steel interface after thermal cycling from our images, due to the dispersion effect as a result of the high density contrast between sealant and steel.

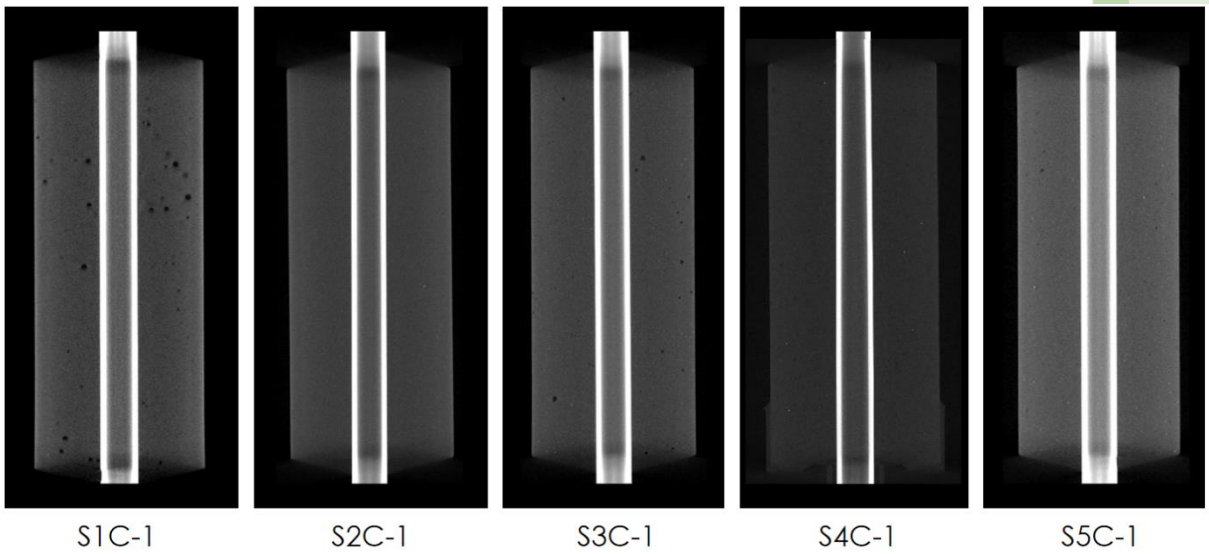

Fig. 8. Micro-CT images of S1 to S5 samples after unconfined thermal-cycling experiments. Voxel resolution of 32 μm. Air is portrayed in black, sealant sheath in grey, steel in white. No cracks are observed in sealant sheath of either sample following thermal treatment. Black pores inside sealant sheath of S1 and S3 samples are pre-existing voids (Li and Pluymakers, 2024a).

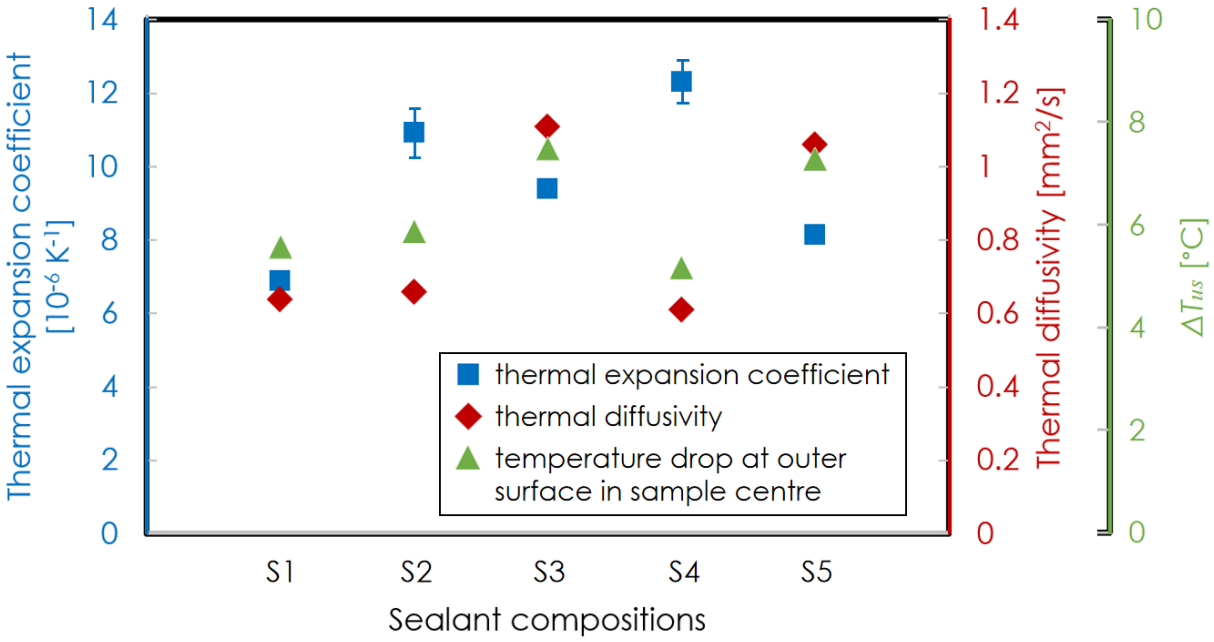

Fig. 9. Thermal expansion coefficient and thermal diffusivity of S1 to S5 sealants, and cycle-averaged temperature drop at outer surface (ΔT_{us}) of S1-S5 sample in unconfined thermal-cycling experiments. The temperature drop is also averaged on measurements of two samples per each sealant.

Figure 9 shows the cycle-averaged temperature drop at outer surface (ΔT_{us}) in unconfined experiments, compared to the thermal expansion coefficient and thermal diffusivity of the five sealants. Compared to S1 and S5, S2 and S4 sealants possess higher thermal expansion coefficient, closer to that of the steel pipe ($15.85\times10^{-6}\,K^{-1}$ for AISI 316L stainless steel, reported by Desai and Ho, 1978). This suggests that the sealant sheath of S2 and S4 would shrink and expand in a similar range as the steel. We interpret this as the main

cause for the less pronounced thermal-induced leaking effects on S2 and S4 compared to S1 and S5 (Fig. 7).

For all sealants, the cycle-averaged temperature drop correlates positively with thermal diffusivity. Note that the thermal diffusivity of the steel pipe is much higher than our sealants (3.43 mm^2/s for AISI 316L stainless steel, measured by Kim, 1975; Ferreira-Oliveira et al., 2022). Increased thermal diffusivity means that a material can conduct heat more efficiently and rapidly during thermal cycling. Despite its moderate thermal expansion coefficient, S3 exhibits the highest. This implies that it can react faster to temperature differences and therefore result in less potential of debonding between sealant and the steel pipe.

Figure 10 shows the tensile strength of the sealants and the cycle-averaged thermal stress on S1 to S5 samples induced in unconfined thermal-cycling experiments. The thermal stress is lower than tensile strength for all sealants indicating that the stress is insufficient to initiate model I cracks (displacement is normal to the cracking plane) by tensile failures (Paterson and Wong, 2005) in the sealant sheath. This is supported by CT images (Fig. 8), and further implies that the observed thermal-induced leaking of all sealants except S3 in unconfined experiments mainly occurred through the sealant-steel interface.

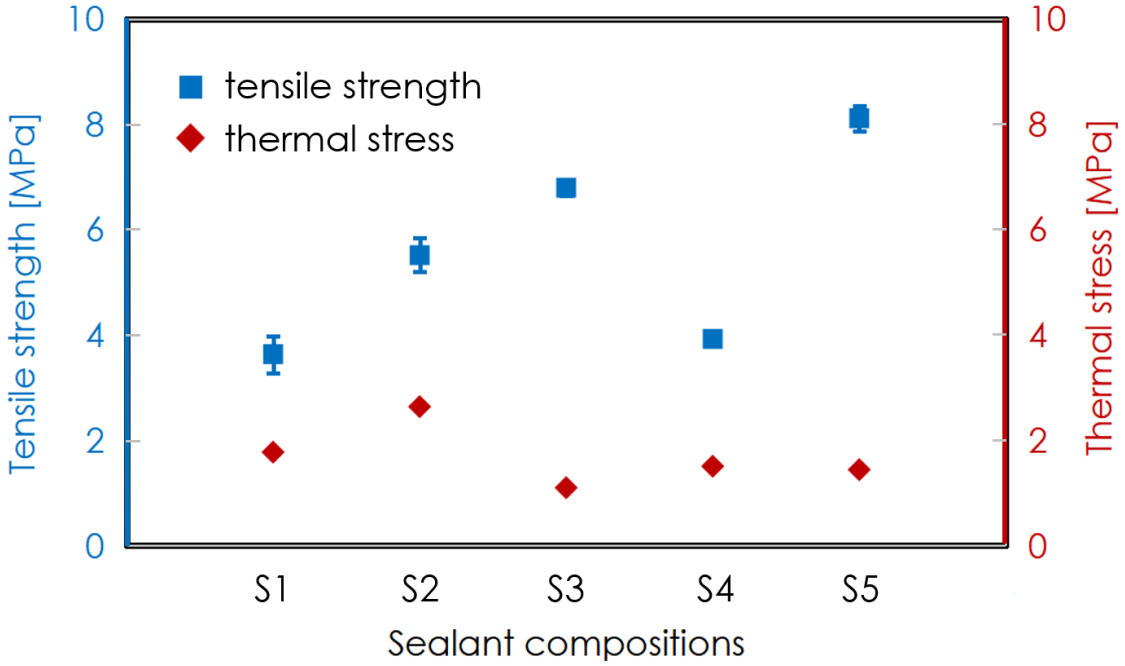

Fig. 10. Tensile strength of S1 to S5 sealants and cycle-averaged thermal stress on their samples induced in unconfined thermal-cycling experiments. The thermal stress is also averaged on measurements of two samples per each sealant.

3.3 Thermo-mechanical behaviour under confined thermal cycling

Figure 11 presents 3 bar N_2 penetration rates of S1 to S5 composite samples before and after confined thermal-cycling experiments. Penetration rates before and after reference confined experiments (without thermal cycling) on S4 and S5 samples (S4C-4 and S5C-4) are also displayed in Fig. 11. The rate decreases after confined thermal treatment for samples of all sealants except S3. The change after thermal treatment for S3 sample is insignificant. These imply a sealing effect by confined thermal cycling on composite samples of all sealants except S3. Compared to S1 and S2, S4 and S5 samples experience greater decrease in penetration rate. After reference experiments on samples S4C-4 and S5C-4 with only confinement but no thermal treatment, the samples also undergo a reduction in the penetration rate indicating that sealing occur on these two samples as well. The penetration rate decrease on all samples except S3C-3 in confined thermal-cycling experiments and confined reference experiments validates that

confinement alone leads to sealing, which dominates over any potential leaking effects induced by thermal cycling. This is confirmed by the overarching compactive trend in circumferential strain under confinement (Fig. 6).

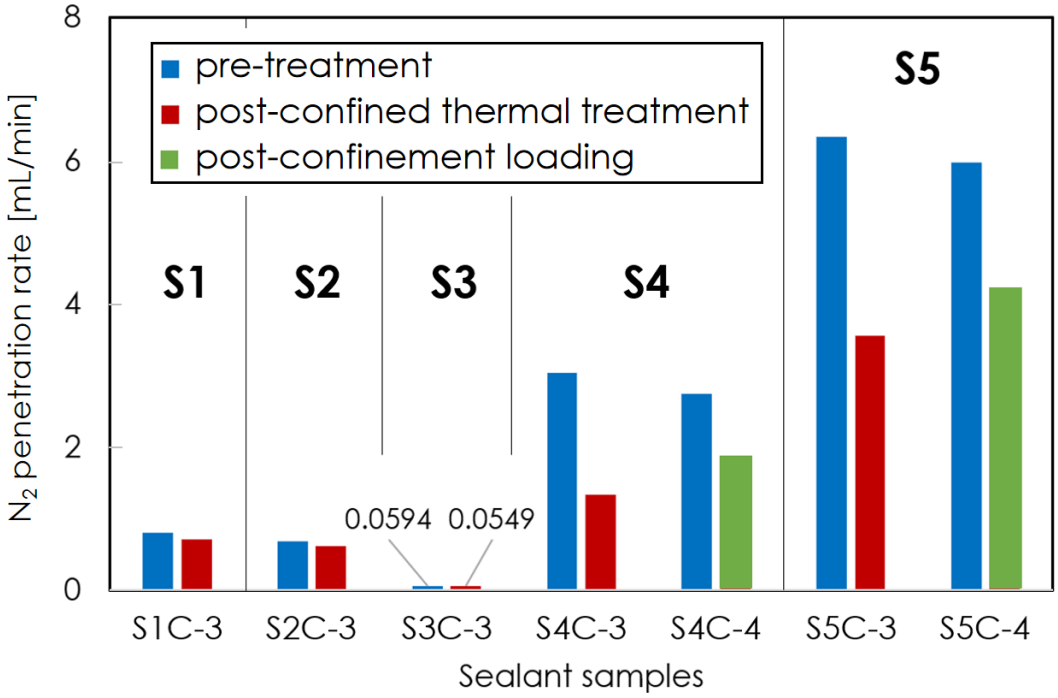

Fig. 11. N_2 penetration rates of composite samples of sealants S1 to S5 (one samples per each sealant) before and after confined thermal-cycling experiments. Penetration rates before and after reference confined experiments (without thermal cycling) on S4 and S5 samples (S4C-4 and S5C-4) are also displayed. Compaction due to confinement is the main reason for the enhanced seal.

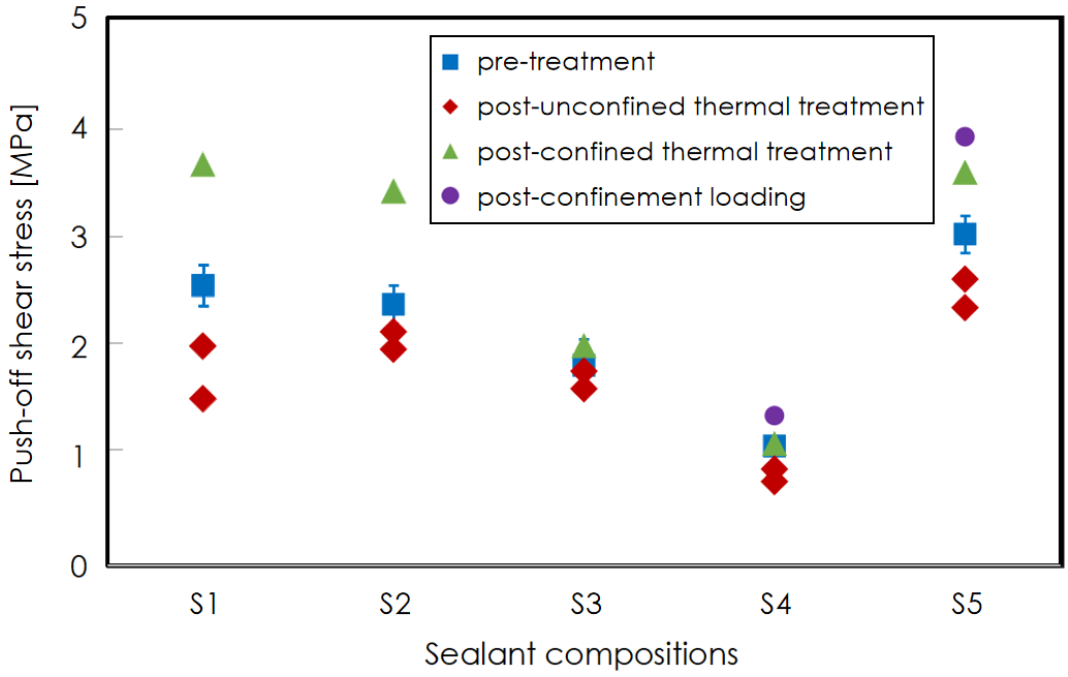

Fig. 12. Push-off shear stress of untreated S1 to S5 composite samples and all other tested samples (listed in Table 3).

3.4 Push-off shear stress of S1 to S5 samples after unconfined and confined thermal cycling

Figure 12 shows the push-off shear stress σ_{po} of untreated S1 to S5 composite samples and all other tested samples listed in Table 3. After unconfined thermal treatment, σ_{po} decreases for all S1 to S5 samples. This implies that the bonding at the sealant-steel interface was deteriorated by unconfined thermal cycling. S1 and S5 samples went through the biggest de-bonding with the greatest reduction in σ_{po}, while S3 samples experienced the least. This reflects the observation in the changes of the N_2 penetration rates in unconfined thermal-cycling experiments (Fig. 7), where the rates increased the most for S1 and S5, and the least for S3.

After confined thermal-cycling experiments, σ_{po} increases for S1, S2 and S5 samples, while it doesn't change for S3 and S4 samples. The σ_{po} also increases for S4 and S5 samples after confined reference experiments. The increase in σ_{po} of samples in these two type of experiments is attributed to enhanced sealing at the sealant-steel interface by confinement, which is also evidenced by the decreased N_2 penetration rates (Fig. 11). Note that the increase in σ_{po} of S1 and S2 samples after confined thermal cycling is the greatest.

Figure 13 shows the Young's modulus of the five sealants and the end-point circumferential strain of S1 to S5 samples after their confined thermal-cycling experiments. Compared to our sealants, the steel pipe is much rigid with a high Young's modulus (200 GPa for AISI 316L stainless steel reported by Rehmer et al., 2023). The deformation of the steel pipe during confined experiment is hence negligible. Compared to other sealants, S1 and S2 possess high Young's modulus, i.e. they are relatively stiff, However, they have undergone the most compaction, i.e. have undergone the most permanent deformation and also exhibit the biggest increase in push-off shear stress, which would imply improved sealing. Moreover, their change in penetration rate was low. So even though the overall sealant sample compacted, the pathways along the steel tubing remained very similar, which could be explained by their high stiffness.

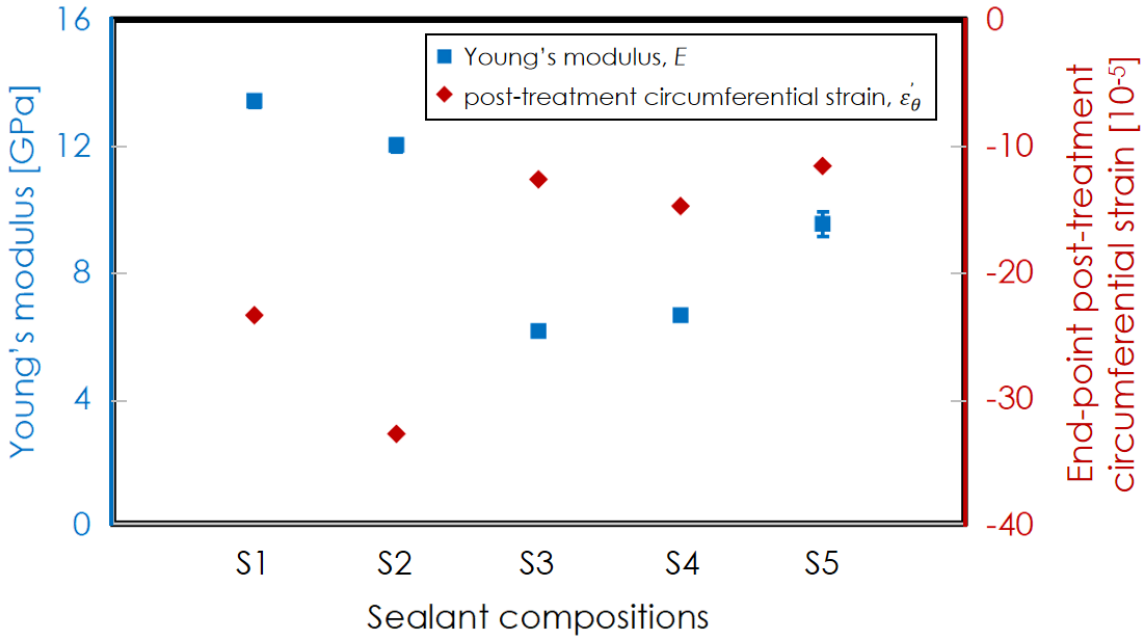

Fig. 13. Young's modulus of the five sealants and the end-point circumferential strain of S1 to S5 samples after their confined thermal-cycling experiments.

3.5 Implications for CO_2 storage

In the context of CCS, two categories of sealants are typically encountered: existing sealant compositions in legacy wells and new sealant designs specifically for CCS conditions. Often, these sealants are OPC-based or similar, with our S1 and S2 sealants as representatives. Our results demonstrate that, in addition

to understanding the mechanical properties, it is crucial to consider the thermal properties of both the sealant and steel to assess the risk of forming leakage pathways along the steel annulus of the wellbore. When the linear expansion coefficient of the sealant is close to that of steel, good bonding at the interface is expected, even if local confinement is low or non-existent. The presence of confinement further reduces the risk of debonding. Drawing from the example of the fracture-resistant S3 in our study, for new sealant designs, apart from any chemical resistance (van Noort et al., 2025), high tensile strength and high thermal diffusivity indicate a lower susceptibility to deterioration by thermal stress accumulation. Such sealants are therefore better suited for CCS environments where thermal cycling is anticipated.

4 Conclusions

This study evaluates the effects of thermal cycling on the thermo-mechanical behaviour of five different sealants (S1 to S5) in simulating the sealant-steel interface of CCS wells. Our results demonstrate that under unconfined conditions, thermal cycling negatively impacts the sealing ability of all sealants except S3, with increased leakage at the sealant-steel interfaces and reduced push-off shear stress. The critical factor influencing the performance is the linear thermal expansion coefficient, where sealants with a coefficient closer to that of steel show better bonding and less damage after thermal cycling. Under confined conditions (1.5 MPa), all sealants exhibit improved performance, with no increase in leakage and, in some cases, higher push-off shear stress post-cycling. Confinement helps to reduce the risk of debonding by enabling the sealant sheath to contract in closer proximity to the steel casing during cooling, thus enhancing sealing integrity. These findings underline the importance of considering both thermal and mechanical properties when designing sealants for CCS applications. Sealants with high tensile strength, high thermal diffusivity, and a thermal expansion coefficient similar to that of steel are recommended for future CCS applications, where temperature fluctuations are expected.

Acknowledgement:

The CEMENTEGRITY project is funded through the ACT program (Accelerating CCS Technologies, Horizon2020 Project No 691712).
Financial contributions from the Research Council of Norway (RCN), the Netherlands Enterprise Agency (RVO), the Department for Energy Security & Net Zero (DESNZ, UK), and Harbour Energy are gratefully acknowledged.

We thank Jan Etienne, Ellen Meijvogel-de Koning, and Jens van den Berg in Geoscience & Engineering Laboratory at Delft University of Technology, the Netherlands, for their technical support.

References

Albawi, A., De Andrade, J., Torsæter, M., Opedal, N., Stroisz, A., & Vrålstad, T. (2014, February). Experimental set-up for testing cement sheath integrity in arctic wells. In OTC Arctic Technology Conference. *OnePetro*. https://doi.org/10.4043/24587-MS.

Alnes, H., Eiken, O., Nooner, S., Sasagawa, G., Stenvold, T., & Zumberge, M. (2011). Results from Sleipner gravity monitoring: Updated density and temperature distribution of the CO2 plume. *Energy Procedia*, **4**, 5504-5511. https://doi.org/10.1016/j.egypro.2011.02.536.

American Petroleum Institute. (2009). Recommended Practice for Subsea Production System Reliability and Technical Risk Management. APIRP 17N.

API, R. P. 10b-2 (2013). Api Recommended Practice 10B-2, Recommended Practice for Testing Well Cements. API RP 10B-2.

Barborak, R. (2010). Calcium aluminate cement concrete (class cac concrete) txdot special specification ss-4491 tip sheet. Construction and Bridge Divisions, Texas Department of Transportation: Austin, TX, USA.

Callister, W. D., Rethwisch, D. G., Blicblau, A., Bruggeman, K., Cortie, M., Long, J., ... & Mitchell, R. (2007). Materials science and engineering: an introduction (Vol. **7**, pp. 665-715). New York: John wiley & sons.

Carey, J. W., Wigand, M., Chipera, S. J., WoldeGabriel, G., Pawar, R., Lichtner, P. C., Wehner, S. C., Raines, M. A., & Guthrie Jr, G. D. (2007). Analysis and performance of oil well cement with 30 years of CO2 exposure from the SACROC Unit, West Texas, USA. *International journal of greenhouse gas control*, **1**(1), 75-85. https://doi.org/10.1016/S1750-5836(06)00004-1.

Carter, G. F., & Paul, D. E. (1991). Materials science and engineering. *ASM international*.

Celia, M. A., Bachu, S., Nordbotten, J. M., Gasda, S. E., & Dahle, H. K. (2005). Quantitative estimation of CO2 leakage from geological storage: Analytical models, numerical models, and data needs. *In Greenhouse Gas Control Technologies* **7** (pp. 663-671). Elsevier Science Ltd. https://doi.org/10.1016/B978-008044704-9/50067-7.

De Andrade, J., Sangesland, S., Todorovic, J., & Vrålstad, T. (2015, April). Cement sheath integrity during thermal cycling: a novel approach for experimental tests of cement systems. In SPE Bergen one day seminar. *OnePetro*. https://doi.org/10.2118/173871-MS.

Desai, P. D., & Ho, C. Y. (1978). Thermal linear expansion of nine selected AISI stainless steels. *Cindas report*, 51.

Dugonjic-Bilic, F., Tiemeyer, C., & Plank, J. (2011, April). Study on admixtures for calcium aluminate phosphate cement useful to seal CCS wells. In SPE International Symposium on Oilfield Chemistry. *OnePetro*. https://doi.org/10.2118/141179-MS.

Eiken, O., Ringrose, P., Hermanrud, C., Nazarian, B., Torp, T. A., & Høier, L. (2011). Lessons learned from 14 years of CCS operations: Sleipner, In Salah and Snøhvit. *Energy procedia*, **4**, 5541-5548. https://doi.org/10.1016/j.egypro.2011.02.541.

Fatemi, A., & Yang, L. (1998). Cumulative fatigue damage and life prediction theories: a survey of the state of the art for homogeneous materials. *International journal of fatigue*, **20**(1), 9-34.

Ferreira-Oliveira, J. R., De Lucena, L. R. R., Dos Reis, R. P. B., De Araújo, C. J., & Bezerra-Filho, C. R. (2022). Thermal diffusivity measurement of stainless-steel alloys through use of the Angstrom's method. *Experimental Heat Transfer*, **35**(4), 419-439.

Freire, A. L., José, H. J., & Moreira, R. D. F. P. M. (2022). Potential applications for geopolymers in carbon capture and storage. *International Journal of Greenhouse Gas Control*, **118**, 103687.

Hajiabadi, S. H., Khalifeh, M., Van Noort, R., & Silva Santos Moreira, P. H. (2023). Review on geopolymers as wellbore sealants: state of the art optimization for CO2 exposure and perspectives. *ACS omega*, **8**(26), 23320-23345.

Hajiabadi, S. H., Li, K., Pluymakers, A., van Noort, R., & Khalifeh, M. (2024). Exploring the Durability of a Granite-Based Geopolymer Sealant for Carbon Capture and Storage: Evaluating Sealing Performance Under Thermal Shocks in Brine Environments. Available at SSRN 5010201.

Kim, C. S. (1975). Thermophysical properties of stainless steels (No. ANL-75-55). Argonne National Lab., Ill.(USA).

Kirby, G. A., Chadwick, R. A., & Holloway, S. (2001). Depth Mapping and Characterisation of the Utsira Sand Saline Aquifer, Central and Northern North Sea: *British Geological Survey Report* CR/01/218N. British Geological Survey.

Kvassnes, A., & Clausen, J. A. (2020). U.S. Patent No. 10,774,001. Washington, DC: U.S. Patent and Trademark Office.

Kvassnes, A., & Clausen, J. A. (2021). U.S. Patent No. 11,014,851. Washington, DC: U.S. Patent and Trademark Office.

Lescanne, M., Hy-Billiot, J., Aimard, N., & Prinet, C. (2011). The site monitoring of the Lacq industrial CCS reference project. *Energy Procedia*, **4**, 3518-3525. https://doi.org/10.1016/j.egypro.2011.02.279.

Lesti, M., Tiemeyer, C., & Plank, J. (2013). CO2 stability of Portland cement based well cementing systems for use on carbon capture & storage (CCS) wells. *Cement and concrete research*, **45**, 45-54. https://doi.org/10.1016/j.cemconres.2012.12.001.

Li, K., & Pluymakers, A. M. (2024a). Effects of thermal shocks on integrity of existing and newly-designed sealants for CCS applications. *International Journal of Greenhouse Gas Control*, **133**, 104103. https://doi.org/10.1016/j.ijggc.2024.104103.

Li, K., & Pluymakers, A. (2024b) Confined Thermal Cycling on Sealants with Different Thermomechanical Properties for Ccs. Available at SSRN 5043588.

Lund, H., Torsæter, M., & Munkejord, S. T. (2015, April). Study of thermal variations in wells during CO2 injection. In SPE Bergen One Day Seminar. OnePetro. https://doi.org/10.2118/173864-MS.

Miner, M. A. (1945). Cumulative damage in fatigue.

Nasvi, M. C. M., Ranjith, P. G., Sanjayan, J., & Bui, H. (2014). Effect of temperature on permeability of geopolymer: A primary well sealant for carbon capture and storage wells. *Fuel*, **117**, 354-363.

Parker, M. E., Meyer, J. P., & Meadows, S. R. (2009). Carbon dioxide enhanced oil recovery injection operations technologies. *Energy Procedia*, **1**(1), 3141-3148. https://doi.org/10.1016/j.egypro.2009.02.096.

Paterson, M. S., & Wong, T. F. (2005). Experimental rock deformation: the brittle field (Vol. 348). Berlin: Springer.

Rehmer, B., Bayram, F., Ávila Calderón, L. A., Mohr, G., & Skrotzki, B. (2023). Elastic modulus data for additively and conventionally manufactured variants of Ti-6Al-4V, IN718 and AISI 316 L. *Scientific Data*, 10(1), 474.

Roy, P., Walsh, S. D., Morris, J. P., Iyer, J., Hao, Y., Carroll, S., ... & Torsæter, M. (2016, June). Studying the impact of thermal cycling on wellbore integrity during CO2 injection. In 50th US Rock Mechanics/Geomechanics Symposium. *OnePetro*.

Suresh, S. (1998). Fatigue of materials. *Cambridge University Press* google schola, **2**, 1-7.

van Noort, R., Pluymakers, A., Li, K., Suryanto, B., & Starrs, G. (2024a). Development of Tailored Wellbore Sealants for CCS and Other Geological Storage Applications. *First Break*, **42**(9), 89-94.

van Noort, R., Gupta, M., Hajiabadi, S. H., Khalifeh, M., Kvassnes, A., Li, K., ... & Ye, G. (2024b, October). Development and Testing of Novel Cement Designs For Enhanced CCS Well Integrity. In 17th Greenhouse Gas Control Technologies Conference.

van Noort, R., Svenningsen, G., Li, K., & Pluymakers, A. (2025, submitted). Exposure of five cementitious sealant materials to wet supercritical CO2 and CO2-saturated water under simulated downhole conditions. *International Journal of Greenhouse Gas Control*.

Vilarrasa, V., & Rutqvist, J. (2017). Thermal effects on geologic carbon storage. *Earth-science reviews*, **165**, 245-256. https://doi.org/10.1016/j.earscirev.2016.12.011.

Yoo, B. Y., Choi, D. K., Kim, H. J., Moon, Y. S., Na, H. S., & Lee, S. G. (2013). Development of CO2 terminal and CO2 carrier for future commercialized CCS market. *International Journal of Greenhouse Gas Control*, **12**, 323-332. https://doi.org/10.1016/j.ijggc.2012.11.008.